Cell Biochemistry and Biophysics (2023) 81:795–811
https://doi.org/10.1007/s12013-023-01177-6

ORIGINAL PAPER

Impact of Interdependent Ca^{2+} and IP_3 Dynamics On ATP Regulation in A Fibroblast Model

Ankit Kothiya[1] · **Neeru Adlakha**[1]

Accepted: 12 September 2023 / Published online: 25 September 2023

Abstract
The vital participation of Ca^{2+} in human organ functions such as muscular contractions, heartbeat, brain functionality, skeletal activity, etc, motivated the scientists to thoroughly research the mechanisms of calcium (Ca^{2+}) signalling in distinct human cells. Ca^{2+}, inositol triphosphate (IP_3), and adenosine triphosphate (ATP) play important roles in cell signaling and physiological processes. ATP and its derivatives are hypothesized to be important in the pathogenic process that leads to fibrotic illnesses like fibrosis. Fluctuations in Ca^{2+} and IP_3 in a fibroblast cell influence ATP production. To date, no evidence of coupled Ca^{2+} and IP_3 mechanics regulating ATP generation in a fibroblast cell during fibrotic disease has been found. The current work suggests an integrated mechanism for Ca^{2+} and IP_3 dynamics in a fibroblast cell that regulates ATP generation. Simulation has been carried out using the finite element approach. The mechanics of interdependent systems findings vary dramatically from the results of basic independent system mechanics and give fresh information about the two systems' activities. The numerical results provide new insights into the impacts of disturbances in source influx, the *serca* pump, and buffers on interdependent Ca^{2+} and IP_3 dynamics and ATP synthesis in a fibroblast cell. According to the findings of this study, fibrotic disorders cannot be attributed solely to disruptions in the processes of calcium signaling mechanics but also to disruptions in IP_3 regulation mechanisms affecting the regulation of calcium in the fibroblast cell and ATP release.

Keywords Reaction-diffusion equations · ATP · Ca^{2+} dynamics · Fibroblast cell · Finite element approach

Introduction

Ca^{2+} is an essential signaling ion in many biological processes and activities across various tissues and animals. Ca^{2+} signaling is crucial for a number of cellular processes in fibroblast cells, including proliferation, migration, myofibroblast differentiation and extracellular matrix (*ECM*) production. Dysregulation of Ca^{2+} signaling may contribute to the development of fibrotic diseases [1].

G-protein-coupled receptors (*GPCRs*) are proteins found on the surface of fibroblast cell [2]. When a neurotransmitter or signal molecule connects to a *GPCR*, the *GPCR*'s shape changes. This modification activates a G protein that is linked to a *GPCR*. This G protein serves as a messenger, allowing the signal to be sent farther. The activated G protein subsequently interacts with a phospholipase C (*PLC*) effector enzyme. This interaction causes the synthesis of IP_3. IP_3 serves as a backup messenger [3]. It goes throughout the cell in search of its target, the endoplasmic reticulum (*ER*), a compartment within the cell that stores calcium ions. IP_3 binds to particular receptors on the *ER* membrane when it enters the *ER*. This binding leads the *ER* to release calcium ions that have been held in the cell's cytoplasm [4, 5]. In fibroblast cells, IP_3 has a significant impact in mediating various cellular processes including differentiation, migration cell, proliferation and survival. Specifically, IP_3-mediated Ca^{2+} signaling regulates fibroblast migration and proliferation, which are important processes for wound healing and tissue repair [5].

ATP is a molecule that significantly impacts cellular energy metabolism. *ATP* has also been linked to the pathogenesis of fibrotic disorders. Fibrosis is a pathological disease characterized by an abnormal accumulation of *ECM* proteins leading to tissue scarring and dysfunction [6]. In the context of fibrosis and wound healing, the production

✉ Ankit Kothiya
ankitkothiya1996@gmail.com

[1] DoM, S. V. National Institute of Technology, Surat 395007 Gujarat, India

and degradation of *ATP* play important roles in cellular processes that influence tissue repair and remodeling. During tissue injury or inflammation, cells often experience increased metabolic demands and stress. This can lead to overproduction of *ATP* through processes like glycolysis and oxidative phosphorylation in mitochondria. Overproduction of *ATP* can be influenced by factors such as increased cellular activity, inflammation, and hypoxia [7]. *ATP* is essential for cell migration and proliferation, which are critical for wound healing and tissue repair [8]. *ATP* acts as a signaling molecule and can attract immune cells to the site of injury or inflammation, aiding in the resolution of tissue damage. Overproduction of *ATP* can lead to excessive inflammation and oxidative stress, which can contribute to tissue damage and exacerbate fibrosis [9]. High levels of extracellular *ATP* can activate purinergic receptors on fibroblasts and other cells, promoting fibrosis by stimulating collagen production and fibroblast differentiation [10]. *ATP* degradation leads to the production of adenosine, which has vasodilatory and anti-inflammatory properties. Adenosine can promote tissue protection and healing by reducing inflammation and enhancing blood flow to the site of injury [11]. Adenosine can modulate immune responses and promote tissue repair by promoting the differentiation of fibroblasts into myofibroblasts, which are important for wound contraction and matrix deposition. Inefficient *ATP* degradation can result in the accumulation of *ATP* in the extracellular space, leading to sustained activation of purinergic receptors and perpetuating inflammation and scarring in multiple organs, including the lung, heart, kidney and liver [10–12]. Therefore, a surplus of *ATP* and inadequate removal of *ATP* insufficient degradation can leads various illnesses of the fibroblast, including wound healing and fibrosis. As a result, *ATP* can trigger excitotoxicity, which can harm fibroblasts or even kill them. *ATP* pathogenic mechanisms and their roles in fibrotic diseases are still unknown. Therefore, it is essential to make models that show the movements of Ca^{2+} and IP_3 affecting the production of *ATP*.

Modeling keratinocyte-fibroblast interactions during the normal and abnormal wound recovery process is described by Shakti et al. [13]. Droniou et al. [14] investigated a two-dimensional tumor development model with shifting boundaries that were numerically solved. Using the idea of advection-diffusion, Simpson et al. [15] investigated the contributions of directed and random motility in a fibroblast cell migration test induced by an electric field. Michell [16] proposed a link between high intracellular Ca^{2+} and PIP_2 catabolism. Berridge and Irvine [3] discovered IP_3 to be a second messenger that mobilizes Ca^{2+} from the *ER*. Regarding cellular transmitter release, Fogelson and Zucker [17] proposed the model of presynaptic diffusion of Ca^{2+} that includes inflow, cytoplasmic binding and surface pumps. Jafri and Keizer [18] examined Ca^{2+} transport in the cell cytosol and Ca^{2+} handling by the *ER* in their study of IP_3-induced Ca^{2+} wave propagation.

Smith et al. [19] developed a reaction-diffusion model describing Ca^{2+} transport with diffusion, source influx, and buffer mechanisms. The reaction model for calcium buffering has been described in fibroblast cells [20, 21]. Wagner and Keizer [22] studied the effects of fast buffers on Ca^{2+} transport and fluctuation. Kotwani and Adlakha [23] developed a reaction-diffusion model to study effect of buffer binding affinity, diffusion and source amplitude in fibroblast cells. Kotwani and Adlakha [24] investigated a computational model of calcium distributions with source fluxes, *serca*, and buffer approximations in a fibroblast cell. Sun et al. [25] constructed a dynamic model for intracellular calcium responses in a fibroblast cell induced by electrical stimulation.

Manhas and Pardasani [26] proposed a probable mechanism for Ca^{2+} fluctuations based on the interaction of the cell's three Ca^{2+} stores like mitochondria, cytosol and *ER*. Manhas and Pardasani [27] created a mathematical model to investigate the IP_3 kinetics-based Ca^{2+} fluctuations in pancreatic acinar. Jha and Adlakha [28] created a two-dimensional unsteady state model of Ca^{2+} concentration change in neurons. Joshi and Jha [29] analyze the physiological involvement of calbindin-D28k and *VGCC* in Parkinson's disease using a mathematical model that incorporates all key factors such as diffusion coefficient and fluxes. Joshi and Jha [30] created a mathematical model based on the Hilfer fractional reaction-diffusion equation to investigate Ca^{2+} transport in cells. Jha and Adlakha [31] conducted two-dimensional finite element simulations of unsteady state Ca^{2+} diffusion in neurons with a *ER* leak and a *serca* pump. Jha and Adlakha [32] sought to investigate the impact of sodium-Ca^{2+} exchangers and source geometry on the dynamics of Ca^{2+} in a neuron cell. Tewari and Pardasani [33] investigated the oscillations in Ca^{2+} caused by dynamically changing membrane potential, focusing on the sodium pump. Pathak and Adlakha [34] created a two-dimensional model of Ca^{2+} distribution in myocytes, including excess buffer approximation, diffusion and point source. In a one-dimensional instance, Naik and Pardasani [35] investigated the influence of the *serca* pump and ryanodine receptor (*RyR*) on the Ca^{2+} profile in oocytes. For a one-dimensional unstable state situation, Naik and Pardasani [36] created a finite element model of Ca^{2+} distribution in oocytes. Naik and Pardasani [37] used a three-dimensional finite element model to investigate the spatio-temporal Ca^{2+} distribution in oocytes. Kotwani et al. [38] created a two-dimensional unsteady state Ca^{2+} distribution model in fibroblast cells. Kothiya and Adlakha [39] developed a model to investigate the function of Ca^{2+} signaling in the production of IP_3 and *ATP* in fibroblast cells. Jha

et al. [40] use *FEM* to investigated the cytosolic Ca^{2+} concentration distribution in astrocytes in a two-dimensional steady-state situation with excess buffer. Jagtap and Adlakha [41] used finite volume and Crank Nicolson simulations to investigate the advection-diffusion of Ca^{2+} in a hepatocyte cell. *ATP* interacts with P_2Y purinergic receptors in the cell membrane, activating *PLC*, which catalyses IP_3 synthesis from PIP_2. IP_3 interacts synergistically with Ca^{2+} in receptors on the surface of the endoplasmic reticulum (*ER*) and opens channels that allow Ca^{2+} ions to be secreted into the cytoplasm. Ca^{2+} promotes and inhibits its own release. The huge Ca^{2+} concentration gradient also causes a Ca^{2+} leak. An *ATP*-dependent pump returns Ca^{2+} to the *ER*. As a result of this cascade, *ATP* is released into the extracellular space. The study of Stamakis and Mantzaris [42] provides two ideas concerning *ATP* release: Ca^{2+}-regulated or IP_3-regulated *ATP* synthesis.

Let's go further into the physiological dynamics of *ATP* synthesis, concentrating on the interaction between adenosine generation via de novo purine and salvage pathways, as well as the mitochondrial *ETC*. *De Novo Purine Pathway and Adenosine Synthesis:* The de novo purine process entails the progressive synthesis of purine bases from simple precursors such as aspartate, carbon dioxide, glutamine, and glycine. The route begins with the creation of the purine ring structure, which is followed by a series of enzymatic activities that result in the production of inosine monophosphate (*IMP*). This is subsequently converted into adenosine monophosphate (*AMP*) through a series of reactions, ultimately leading to *ATP* synthesis during oxidative phosphorylation [43]. *Salvage Pathway for Adenosine Production:* Cells use the salvage process to recycle purine bases (adenine and guanine) from nucleotides and nucleosides produced during *DNA* and *RNA* degradation. This recycling conserves energy and resources by reusing purine components to build new nucleotides. This enzyme catalyzes the cleavage of nucleosides (e.g., adenosine) into their respective purine bases (adenine). Adenine is then converted into adenosine monophosphate (*AMP*) through the addition of a phosphoribosyl group. AMP can subsequently undergo phosphorylation to form adenosine diphosphate (*ADP*) and, ultimately, *ATP* through the process of oxidative phosphorylation in the mitochondria [44]. *Mitochondrial Electron Transport Chain (ETC) andATP Synthesis:* The mitochondrial *ETC* is a crucial component of *ATP* synthesis, occurring within the inner mitochondrial membrane. It involves a series of protein complexes that facilitate electron transport and proton pumping. Electrons obtained from molecules like glucose and fatty acids are shuttled through these complexes, leading to the transfer of electrons along the *ETC*. As electrons move through the complexes, protons (H+ ions) are pumped across the inner mitochondrial membrane, creating a proton gradient. This enzyme complex, also known as Complex V, is embedded in the membrane and harnesses the proton gradient to synthesize *ATP* from *ADP* and inorganic phosphate (*Pi*) through a process called chemiosmotic coupling. As protons flow back into the mitochondrial matrix through *ATP* synthase, the energy generated is used to drive *ATP* synthesis [45].

In mouse fibroblasts, Bryan et al. [46] investigated the dual function of *ATP* in maintaining volume-regulated chloride channels and in regulating the release of Ca^{2+}. Miyoshi et al. [47] looked at how cells die as they age and what role *ATP* plays in apoptosis and necrosis caused by hydrogen peroxide. Astrocytic cells were explored by Stamatakis and Mantzaris [42], who investigated the link between Ca^{2+}-regulated and IP_3-regulated *ATP* production mechanisms. Chen et al. [6] demonstrated that *ATP* activates the P_2Y_2 receptors in fibroblasts of human cardiac muscle and raises their proliferation via increasing cell cycle progression. It also has the additional effect of increasing the migration of cells. These actions of *ATP* may assist in modifying the structure of damaged hearts. Kotwal et al. [48] investigated the essential function *ATP* plays in macrophages as they expedite wound healing and regeneration. One-dimensional mathematical models of *T*-lymphocyte Ca^{2+} distribution were constructed by Kumar et al. [49] using a finite element technique. Source inflow, buffers and *RyR* receptor effects were also acquired for unusual circumstances, and the *serca* pump effects were found for the temporal case. A one-dimensional fractional reaction-diffusion model for *RyR*, *VGCC* and calbindin-D28k was explored by Joshi and Jha [29]. They found analytical answers for Parkinson's brain physiology. Jagtap and Adlakha [50] used the finite volume method to be looked into the cytosolic Ca^{2+} distribution in hepatocyte cells. Joshi et al. [51] investigated intracellular calcium dynamics in fibroblasts using an exponential kernel rule.

Glycolysis is a key metabolic pathway that happens in the cytoplasm of cells and acts as the first step in the breakdown of glucose to create *ATP*. Glycolysis begins with the activation of glucose, a six-carbon sugar. Two molecules of *ATP* are initially invested to convert glucose into fructose-1,6-bisphosphate. The six-carbon sugar molecule is split into two three-carbon molecules: glyceraldehyde-3-phosphate and dihydroxyacetone phosphate. Only glyceraldehyde-3-phosphate continues through the pathway. Glyceraldehyde-3-phosphate undergoes a series of reactions, leading to the production of two molecules of *NADH* (a high-energy electron carrier) and four molecules of *ATP*. However, since two *ATP* molecules were initially invested, there is a net gain of two *ATP* molecules per glucose molecule. The final steps of glycolysis convert each glyceraldehyde-3-phosphate into pyruvate, a three-carbon compound. During this process, an additional two

molecules of *NADH* are produced [52]. *The Tricarboxylic Acid (TCA) Cycle*, often known as the citric acid cycle or Krebs cycle, is a major metabolic system that occurs in eukaryotic cell mitochondria and prokaryotic cell cytoplasm. It is an essential component of respiration in cells and helps to generate energy in the form of *ATP*. The *TCA* cycle begins when acetyl coenzyme A (Acetyl-CoA) enters the cycle. Acetyl-CoA is derived from various sources, including the breakdown of carbohydrates, fats, and amino acids. The acetyl group from Acetyl-CoA is combined with a four-carbon compound called oxaloacetate to form citrate. Citrate undergoes a series of enzyme-catalyzed reactions, including isomerization and dehydration, leading to the regeneration of isocitrate. It is further oxidized by the enzyme isocitrate dehydrogenase, resulting in the release of carbon dioxide (CO_2) and the formation of α-ketoglutarate. This step also generates reduced nicotinamide adenine dinucleotide (*NADH*), a carrier molecule that stores high-energy electrons [53]. α-Ketoglutarate is then oxidized by the enzyme α-ketoglutarate dehydrogenase complex, producing another molecule of CO_2 and another molecule of *NADH*. The resulting molecule, succinyl-CoA, also captures high-energy electrons. Succinyl-CoA undergoes a series of reactions that ultimately lead to the formation of succinate. This step releases a molecule of guanosine triphosphate (*GTP*), which is a molecule similar to *ATP* and can be readily converted into *ATP*. Succinate is further oxidized by the enzyme succinate dehydrogenase, which is embedded in the inner mitochondrial membrane and also serves as a part of the *ETC*. This oxidation generates another molecule of FADH2, another carrier molecule storing high-energy electrons. The oxidation of succinate produces fumarate. This step involves the addition of water to the double bond of succinate. Fumarate is then enzymatically converted to malate. Malate is oxidized by the enzyme malate dehydrogenase, producing another molecule of *NADH* and regenerating oxaloacetate. Oxaloacetate can then combine with another acetyl group from Acetyl-CoA to restart the cycle. The reduced electron carriers, *NADH* and *FADH*2, generated during the *TCA* cycle, play a crucial role in *ATP* production. These carriers carry high-energy electrons to the *ETC* located in the inner mitochondrial membrane. As these electrons move through the *ETC*, they establish a proton gradient across the membrane, which creates a flow of protons (H^+) back into the mitochondrial matrix through *ATP* synthase [54]. This flow of protons drives the *ATP* synthase enzyme to synthesize *ATP* from inorganic phosphate (Pi) & *ADP* in a process known as oxidative phosphorylation. The coupling of electron transport and proton pumping in the *ETC* with *ATP* synthesis is termed chemiosmotic coupling. The exact number of *ATP* molecules generated from one round of the *TCA* cycle varies based on factors such as the availability of oxygen and the efficiency of electron transport. However, in total, one round of the *TCA* cycle can contribute to the production of multiple molecules of *ATP* [55].

Several researchers have investigated the interdependence Ca^{2+} and IP_3 dynamics in cells, such as hepatocytes [56], myocyte [57], etc. Some one-way feedback models of Ca^{2+} with other ions like nitric oxide, β-amyloid and dopamine are proposed by Pawar and Pardasani [58–60]. The literature contains models of Ca^{2+} dynamics in fibroblast cells that assume IP_3 as a constant. To make the model more realistic, examine the coupling of Ca^{2+} with other systems' dynamics.

The role of interdependent Ca^{2+} and IP_3 kinetics a in the control of distinct signalling molecules such as nitric oxide, β-amyloid and *ATP* in neurons have been studied by Pawar and Pardasani [61–63]. Recently, feedback model of *NO* generation is regulated by Ca^{2+} and IP_3 in fibroblast cells was developed by Kothiya and Adlakha [64]. Singh and Adlakha [65] investigated the influence of source geometry on the system kinetics of calcium and IP_3 in myocytes of the heart. Joshi et al. [51] established a model to study the impact of buffer and calcium oscillation in fibroblast cells. The effects of buffer, *serca* pump and source influx, on coupled calcium and IP_3 dynamics with insulin secretion in beta cells have been studied by Vaishali and Adlakha [66]. Kothiya and Adlakha [67] developed a two-way feedback model of the system kinetics model of *PLC* and $Ca2^{+}$ incorporating the buffer mechanism, diffusion parameters, source influx, and *serca* rate in a fibroblast cell.

There has been no attempt to investigate the influence of coupled calcium and IP_3 kinetics on the control of *ATP* synthesis. Given the regulatory functions of IP_3, *ATP* and Ca^{2+} ions in fibroblasts and cancer-associated fibroblast (*CAF*), there is a need for knowledge about the effects of IP_3 and Ca^{2+} dynamics on *ATP* synthesis and the cytoprotective and cytotoxic effects of *ATP*. In the past, no such theoretical investigation in this area has been recorded. The goal of this study is to look at the regulatory and deregulatory effects of system mechanics of calcium and IP_3 in fibroblasts that regulate *ATP* synthesis. The findings were derived with the use of the *FEM*. The impact of numerous factors on the paired dynamics of calcium and IP_3, as well as their impacts on *ATP* synthesis, have been investigated. A model is provided here that incorporates a two-way coupling between the Ca^{2+} and IP_3 systems in fibroblast cells to regulate *ATP* levels. It is simulated to disclose information on changes in *ATP* synthesis induced by changes in the amounts of Ca^{2+} and IP_3 in fibroblasts. The coupled dynamics of calcium and IP_3 with a buffer mechanism and ATP release propose to study the role of constitutive processes like buffer, source influx, association rate, etc., in normal and fibrotic conditions.

Mathematical Formulation

By adding buffer terms to the model of Wagner et al. [68] the Ca^{2+} transport in fibroblasts in the presence of IP_3 is expressed as

$$\frac{\partial[Ca^{2+}]}{\partial t} = D_c\left[\frac{\partial^2[Ca^{2+}]}{\partial x^2}\right] + \left[\frac{J_{IP_3R} - J_{serca} + J_{leak}}{F_c}\right] - K^+[B]_\infty\left[[Ca^{2+}] - [Ca^{2+}]_\infty\right]. \quad (1)$$

In this case, $[B]_\infty$ represents the steady-state buffer concentration, while $[Ca^{2+}]_\infty$ represents the steady-state Ca^{2+} ion concentration.The notation D_c denotes the diffusion coefficient of Ca^{2+}. The variable for time is denoted by the letter 't', while the variable for the position is denoted by the letter 'x'. The symbol K^+ represents the rate of buffer association. The influx and outflux terms of equation (1) are given by Keizer et al. [69] as given below,

$$J_{IP_3R} = V_{IP_3R}m^3h^3\left[[Ca^{2+}]_{ER} - [Ca^{2+}]\right], \quad (2)$$

$$J_{serca} = V_{serca}\left[\frac{[Ca^{2+}]^2}{[Ca^{2+}]^2 + K^2_{serca}}\right], \quad (3)$$

$$J_{leak} = V_{leak}\left[[Ca^{2+}]_{ER} - [Ca^{2+}]\right]. \quad (4)$$

Where J_{IP_3R}, J_{leak} and J_{serca} each represent a different flow associated with the IP_3 receptor, the leaking pump and the *serca* pump, respectively. V_{leak} and V_{IP_3R} are the flux rate constants for leak and IP_3 respectively.The maximum rate and the Michaelis constant for the *serca* pump are represented by the variables V_{leak} and V_{IP_3R}, respectively.

The definitions of m and h can be found in Keizer and Young's work [69].

$$m = \left[\frac{[IP_3]}{[IP_3] + K_{IP_3}}\right]\left[\frac{[Ca^{2+}]}{[Ca^{2+}] + K_{Ac}}\right], \quad (5)$$

$$h = \left[\frac{K_{Inh}}{[Ca^{2+}] + K_{Inh}}\right]. \quad (6)$$

K_{IP_3}, K_{Ac} and K_{Inh} are the dissociation constants of IP_3 that activate Ca^{2+} and inhibit Ca^{2+} successively. Here, IP_3 dynamics in the presence of Ca^{2+} described by Wagner et al. [68] is used and might be represented in fibroblasts as;

$$\frac{\partial[IP_3]}{\partial t} = D_I\left[\frac{\partial^2[IP_3]}{\partial x^2}\right] + \left[\frac{J_{production} - \lambda(J_{kinase} + J_{phosphates})}{F_c}\right]. \quad (7)$$

Where $[IP_3]$ shows the cytosolic concentration of IP_3. D_I is IP_3 diffusion coefficient. Wagner et al. [68] gives the Ca^{2+} dependent IP_3 release terms as given below;

$$J_{production} = V_{production}\left[\frac{[Ca^{2+}]}{[Ca^{2+}] + K^2_{production}}\right], \quad (8)$$

Where $K_{production}$ represents the Michaelis constant for calcium activation, $J_{production}$ represents the flux term for IP_3 production and $V_{production}$ represents the maximal IP_3 generation rate. Bugrim et al. [70] and Sims and Allbrittont [71], as noted below, supply the additional flux terms, namely the IP_3 degradation by J_{Kin} and $J_{phosphatase}$.

$$J_{kin} = (1 - \theta 1)V_1\left[\frac{[IP_3]}{[IP_3] + 2.5}\right] + \theta 1 V_2\left[\frac{[IP_3]}{[IP_3] + 1/2}\right], \quad (9)$$

$$J_{phosphatase} = V_3\left[\frac{[IP_3]}{[IP_3] + 30}\right]. \quad (10)$$

$$\theta 1 = \left[\frac{[Ca^{2+}]}{[Ca^{2+}] + (39/100)}\right]. \quad (11)$$

Where V_1, V_3 and V_2 are the maximum rate constants for low calcium (3-kinase), phosphatase and high calcium (3-kinase) respectively. A variable parameter ($\lambda = 30$) estimates the degradation rate [68].

The cell calcium level calculates the Ca^{2+}_{ER} via conversation relationship.

$$[Ca^{2+}]_T = F_E[Ca^{2+}]_{ER} + F_C[Ca^{2+}]_C. \quad (12)$$

Initial Conditions

The following two initial conditions are framed by Brown et al. [72] and Dupont et al. [73] based on the assumption that the cell is initially at rest, having an initial concentration of IP_3 and Ca^{2+}.

$$[IP_3]_{t=0} = 0.16\,\mu M. \quad (13)$$

$$[Ca^{2+}]_{t=0} = 0.1\,\mu M. \quad (14)$$

Boundary Conditions

For Ca^{2+}, the boundary conditions framed by Brown et al. [72] as mentioned below;

$$\left[-D_c\frac{\partial[Ca^{2+}]}{\partial x}\right] \to \sigma,\ as\ x \to 0\,\mu m, \quad (15)$$

where σ represents the source amplitude.

The furthest border from the source is indicated by [74, 75]

$$\lim_{x\to 10}[Ca^{2+}] = [Ca^{2+}]_{\infty} = 0.1\,\mu M. \tag{16}$$

Also, for IP_3 kinrtics, the boundary circumstances given by Fink et al. [76] and Brown et al. [72] as given below.

$$\lim_{x\to 0}[IP_3] = 3\,\mu M, t > 0; \tag{17}$$

$$\lim_{x\to 10}[IP_3] = 0.16\,\mu M. \tag{18}$$

Regulation of Ca^{2+} and IP_3 Dependent *ATP*

The Ca^{2+} and IP_3 regulated *ATP* synthesis is given by Stamatakis and Mantzaris [42] as,

$$J_{release} = \beta P([Ca^{2+}])Q([IP_3]). \tag{19}$$

Where, β is the maximum synthesis rate and $P([Ca^{2+}])$ and $Q([IP_3])$ are the *ATP* release dependent on Ca^{2+} and IP_3 respectively. The Ca^{2+} and IP_3 dependent *ATP* release can be characterized respectively as given below;

$$P([Ca^{2+}]) = \left[\frac{\left(\frac{a_0}{a_0-1}\right) - 2\left(\frac{[Ca^{2+}]}{[Ca^{2+}]_{max}}\right)}{\left(\frac{1}{a_0-1}\right) - \left(\frac{[Ca^{2+}]}{[Ca^{2+}]_{max}}\right)^2}\right]. \tag{20}$$

$$Q([IP_3]) = \left[\frac{\left(\frac{b_0}{b_0-1}\right) - 2\left(\frac{[IP_3]}{[IP_3]_{max}}\right)}{\left(\frac{1}{b_0-1}\right) - \left(\frac{[IP_3]}{[IP_3]_{max}}\right)^2}\right]. \tag{21}$$

Where a_0 and b_0 are constants for *ATP* feedback and $[Ca^{2+}]_{max}$ and $[IP_3]_{max}$ are the cell's maximum Ca^{2+} and IP_3 values. The finite element and Crank Nicholson procedure followed for the solution are given in Appendix.

Results and Discussion

A quantitative solution of the partial differential equations representing the coupled dynamics of IP_3 and Ca^{2+} was achieved using *MATLAB* software. Graphs are employed to visually represent the numerical findings generated by solving the equations. Table 1 shows the numerical measurements of the various parameters used in this study. Figure 1 depicts the systematic pathways of calcium and IP_3 dynamics with the regulation of neurotransmitter ATP production.

Figure 2 depicts the geographic and temporal distributions of Ca^{2+} in fibroblast cells at various periods in time and space. Because the source channel delivers many Ca^{2+} ions into the cell, there may be a high Ca^{2+} distribution at the source $x = 0\,\mu m$. The spatial Ca^{2+} profile lowers from $x = 0\,\mu m$ to $x = 10\,\mu m$ and eventually convergence occurs to the cellular background Ca^{2+} profile ($0.1\,\mu M$). Because the source channel opens, the temporal concentration of Ca^{2+} rises with time in Fig. 2B and the Ca^{2+} level rises in the cytosol of fibroblast cells due to increasing intracellular Ca^{2+} concentration coming from the source. The temporal Ca^{2+} profile achieved equilibrium within 150 *ms* regardless of the cell's location.

Table 1 Physiological variables and their values are listed below [58, 59, 61, 62, 68]

Symbol	Values	Symbol	Values
V_{IP_3R}	$8.5\ s^{-1}$	λ	30
V_{leak}	$0.01\ s^{-1}$	F_c	0.83
$K^+ - EGTA$	$1.5\,\mu M^{-1}s^{-1}$	K_{IP_3}	$0.15\,\mu M$
K_{Ac}	$0.8\,\mu M$	V_{leak}	$0.01\ s^{-1}$
V_{serca}	$0.65\ \mu Ms^{-1}$	K_{serca}	$0.4\,\mu M$
$V_{production}$	$0.075\ \mu Ms^{-1}$	$K_{production}$	$0.4\ \mu M$
V_{Ki1}	$0.001\ \mu Ms^{-1}$	V_{Ki2}	$0.005\ \mu Ms^{-1}$
V_{ph}	$0.02\ \mu M/s$	$[Ca^{2+}]_{\infty}$	$0.1\ \mu M$
D_c	$16\,\mu m^2 s^{-1}$	D_I	$283\,\mu m^2 s^{-1}$

Figure 3 displays the *ATP* release which is Ca^{2+}-dependent for the different time points and positions. The impact of Ca^{2+} concentration on *ATP* release is significant in situations where Ca^{2+} is high. The *ATP* release is also high wherever Ca^{2+} profile is high in the fibroblast cell. The Ca^{2+} distribution is generally high near the source. The *ATP* release is also high at $x = 0\,\mu m$. In Fig. 2B, it has been seen that Ca^{2+} concentration gets a steady state in 150 *ms*. In Fig. 3B, the *ATP* release achieves a steady state in 150 *ms*. This implies that the *ATP* release directly depends on Ca^{2+} concentration in the cell.

Figure 4 displays the spatiotemporal profile of IP_3 profile at various times and places in fibroblasts. In Fig. 4A, the profile of IP_3 goes down ($x = 0$ to $x = 10$) and ends up at a concentration of $0.16\,\mu M$ in the cell. The IP_3 particles stick together near the IP_3 receptor and achieve it's border value ($3\,\mu M$ at $x = 0\,\mu m$) for time $t = 0, 5, 10, 20, 50, 100$ and 1000 *ms* in the fibroblast cell. In Fig. 4A it is observed that IP_3 dynamics is nonlinear initially and approaches a linear behavior after the passage of time reaching a steady state condition. This nonlinearity is due to an imbalance among the various processes of the cell and as these processes achieve equilibrium, the behavior of the profile becomes linear. Figure 4B shows the profile of time of IP_3 distribution which increases with time for various places $x = 0.25, 0.50, 0.75, 1, 2, 5$ & $10\,\mu m$ synergetically with the increase in Ca^{2+} with time in Fig. 2B.

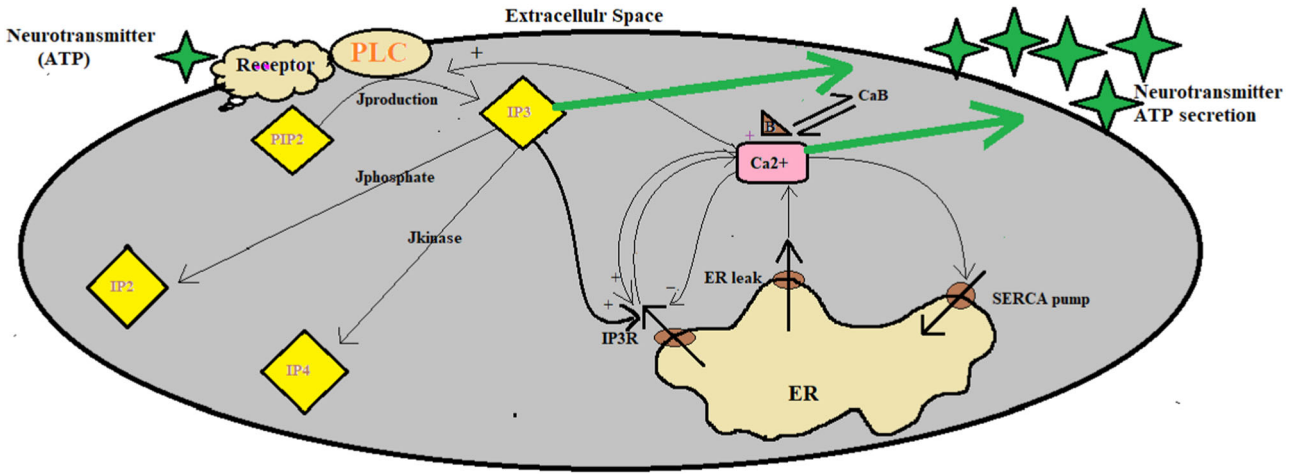

Fig. 1 The schematic diagram reprents the calcium and IP_3 mechanism with ATP release

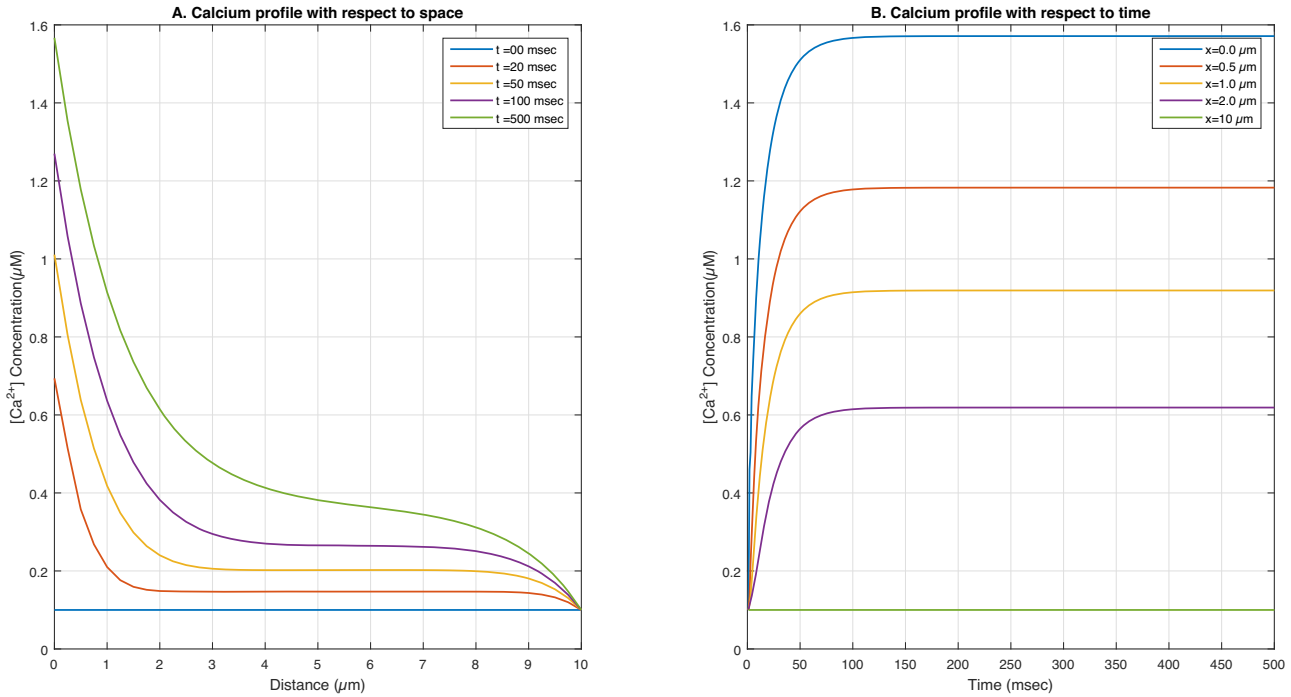

Fig. 2 The Ca^{2+} profile in a fibroblasts at different periods and places for $[B] = 5\,\mu m$, $D_c = 16\,\mu m^2/s$ and $\sigma = 15pA$. A The spatial distribution of calcium and **B** the temporal distribution of calcium

Figure 5 displays the Ca^{2+} distribution at $x = 5\,\mu m$ for $[B] = 400\,\mu M$ under fibrotic conditions in cell. The fluctuation in the temporal profile of Ca^{2+} is observed for greater buffer levels in the cell at the initial time. This damping fluctuation is due to an imbalance among the various processes of the cell and the buffer binds the Ca^{2+} ions and lowers the level of Ca^{2+} concentration in the cell. In Fig. 5A, we found substantial differences in the Ca^{2+} profiles of normal fibroblasts and CAF, though the behavior of the curves is similar in both cases. The oscillation in the Ca^{2+} profile in Fig. 5A is due to the substantial imbalances among the regulatory processes that exist up to $20\,ms$ and then achieve equilibrium. Similarly, in Fig. 5B, the synergetic changes in ATP level are observed like those in Fig. 5A. The spatiotemporal Ca^{2+} concentrations are higher (30%) in the case of cystic fibrosis than in normal fibroblasts [77], As a result, an increased level of Ca^{2+} concentration is hazardous and can lead to fibrosis [78].

Figure 6 shows the IP_3 dependent ATP release for different times and positions. In Fig. 4A, it was seen that IP_3 is highest at $x = 0\,\mu m$ and decreases as we move away from

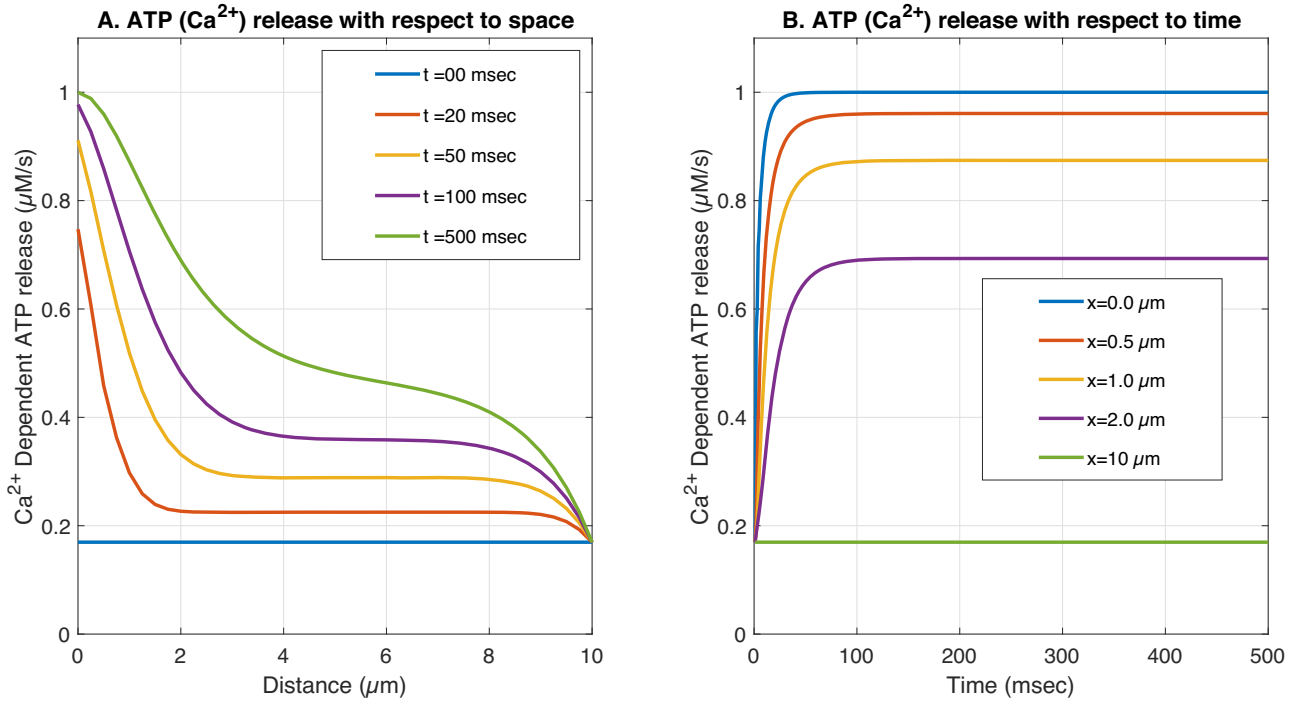

Fig. 3 Ca^{2+} **dependent** ATP **release for various position and time for** $\sigma = 15pA$**. A** The spatial profile of calcium-dependent ATP release and **B** the temporal profile of calcium-dependent ATP release

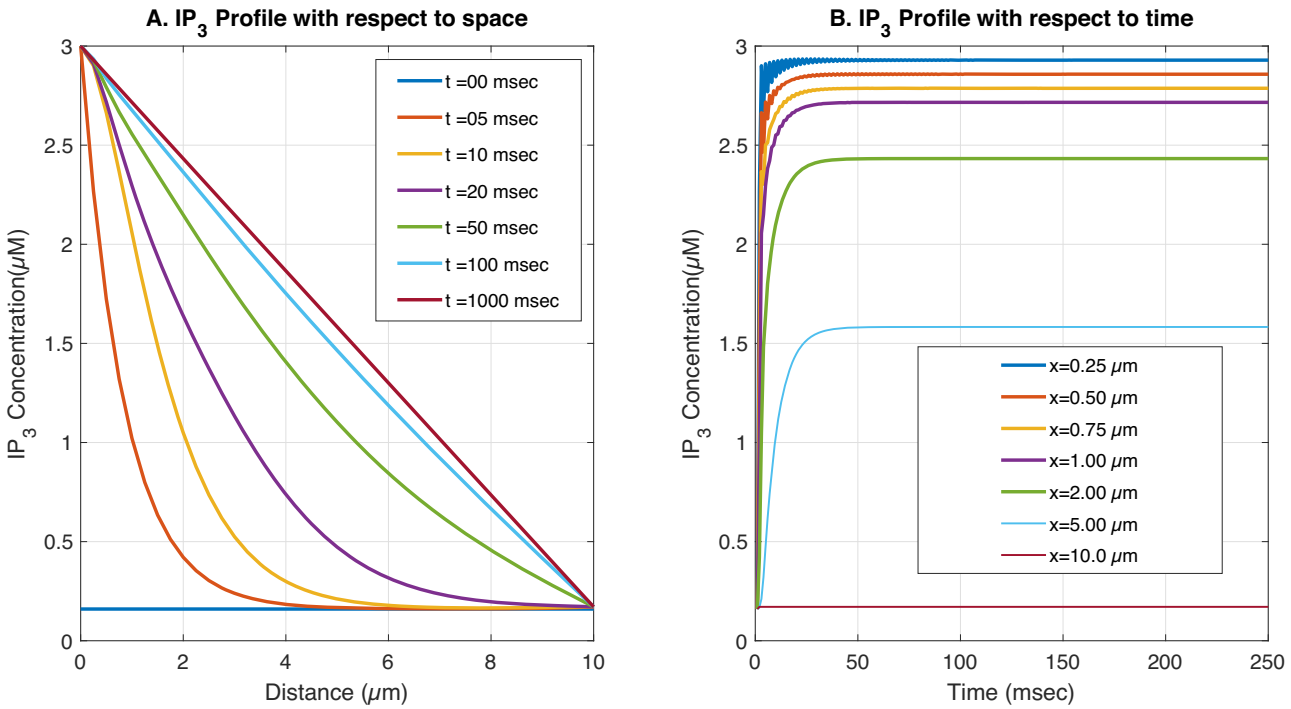

Fig. 4 IP_3 **distribution for various time and position for** $D_c = 16\mu m^2/s$ **and** $\sigma = 15pA$**. A** The spatial distribution of IP_3 and **B** the temporal distribution of IP_3

$x = 0\,\mu m$ to $x = 10\,\mu m$. Similarly in Fig. 6A, we observe that ATP release is highest at $x = 0\,\mu m$ and reduces as it departs from the source. We observed that the behavior of the IP_3 profile changed from nonlinear to linear with the increment of time steps. Also from Fig. 6A, it is observed that the nonlinear behavior of IP_3-dependent ATP has

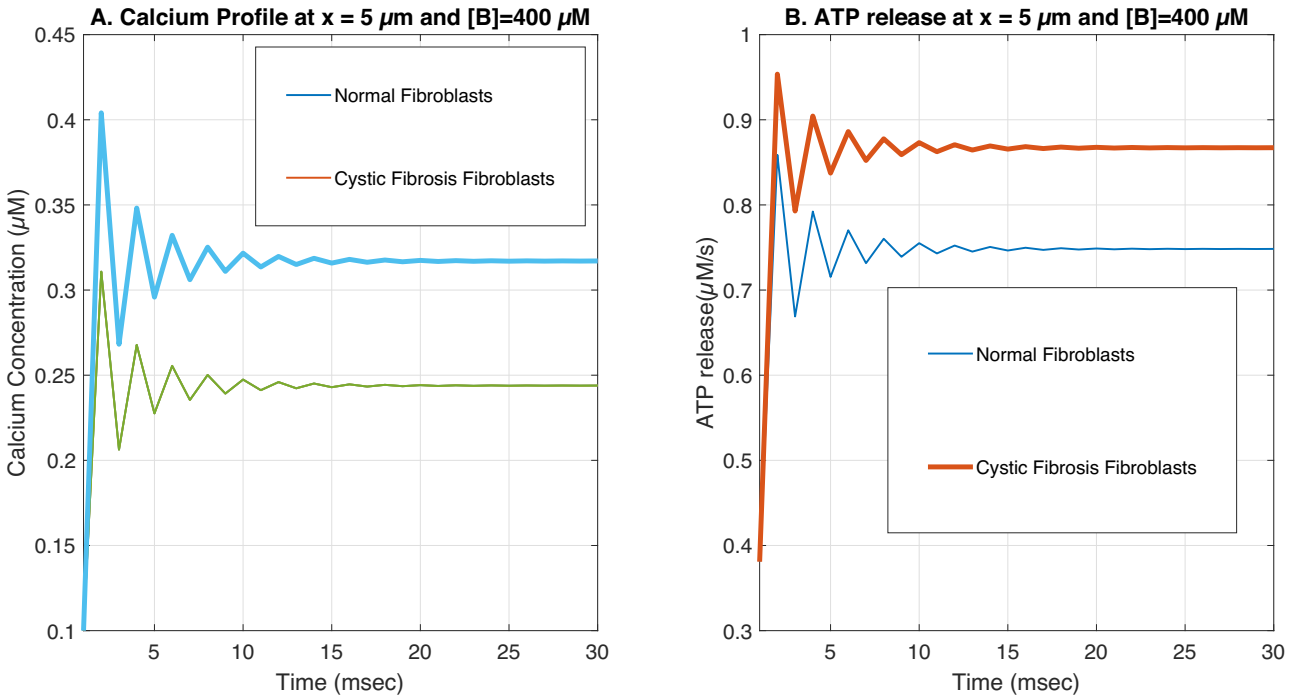

Fig. 5 Ca^{2+} **concentration and** Ca^{2+} **dependent ATP release in a fibroblasts for the buffer concentration** $[B] = 400\,\mu M$ **at** $x = 5\,\mu m$ **with the fibrotic conditions. A** The temporal distribution of calcium in normal and cystic fibrosis fibroblast and **B** the temporal distribution of calcium-regulated ATP in normal and cystic fibrosis fibroblast

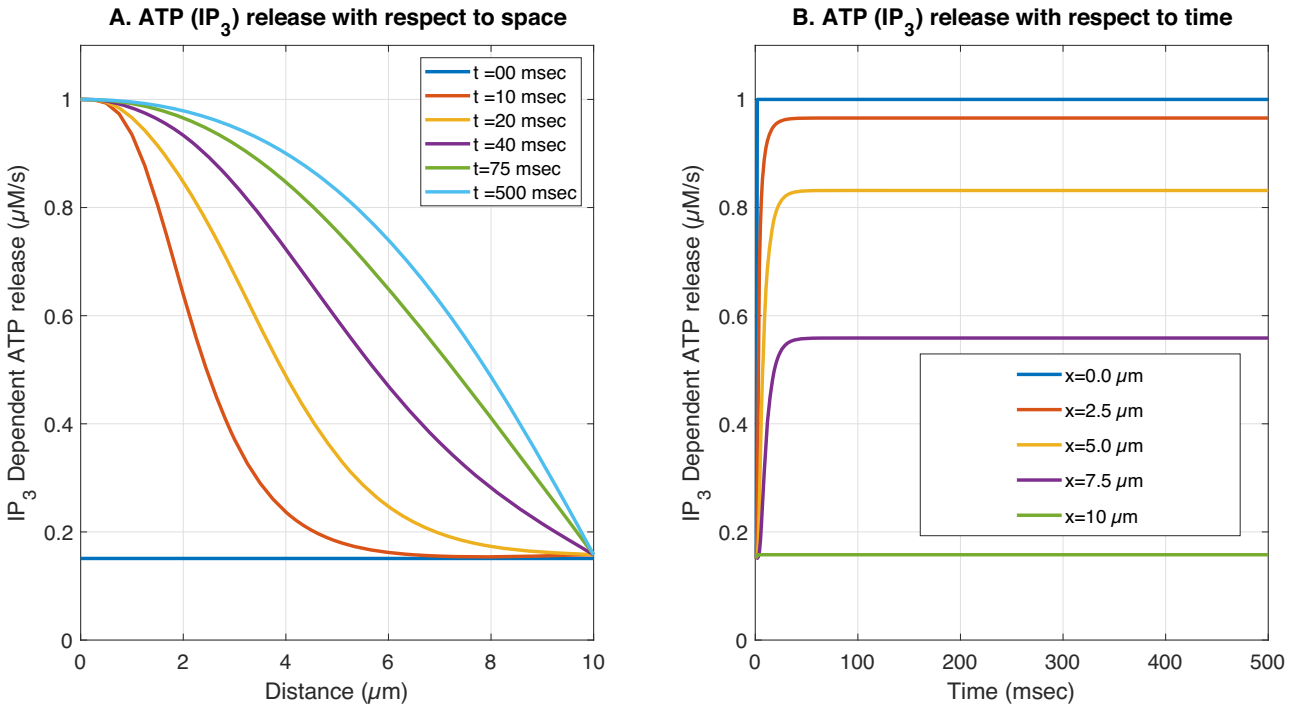

Fig. 6 IP_3 **dependent** ATP **release for various position and time for** $D_c = 16\,\mu m^2/s$ **and** $\sigma = 15pA$**. A** The spatial distribution of IP_3-dependent ATP release and **B** the temporal distribution of IP_3-dependent ATP release

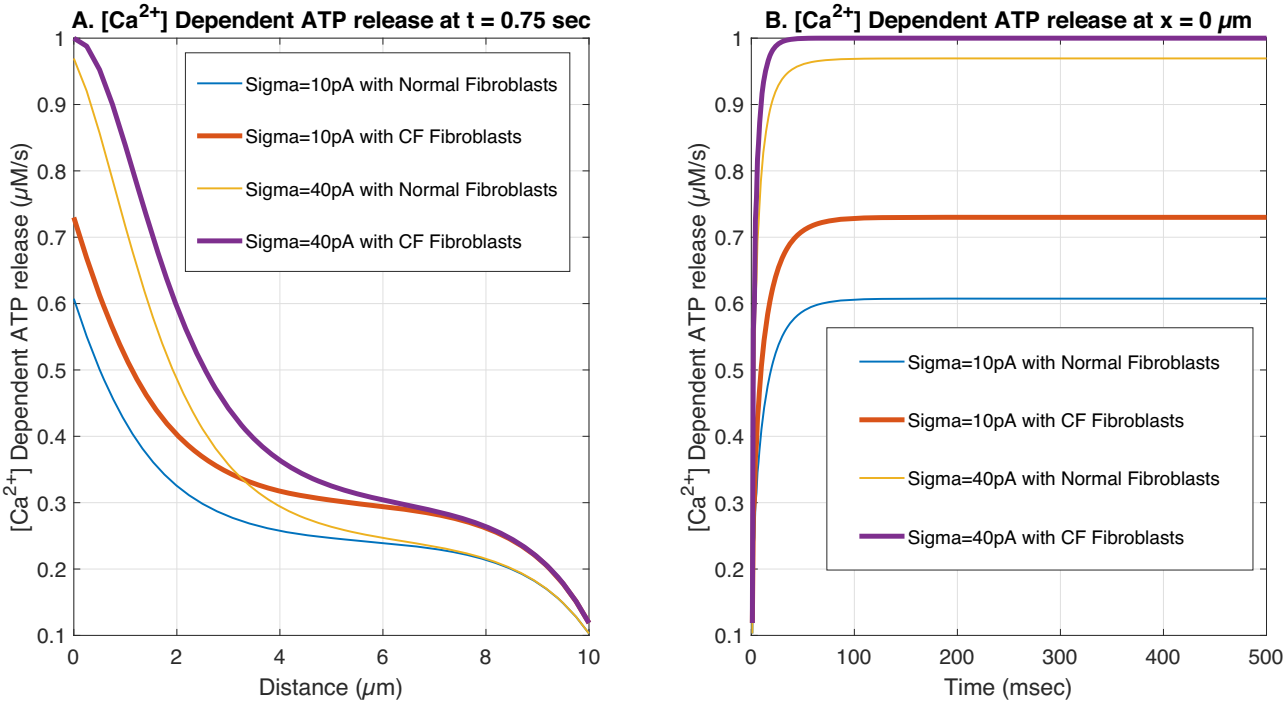

Fig. 7 Ca^{2+} **dependent** *ATP* **release for various source influx for** $[B] = 5\,\mu M$ **and** $D_c = 16\,\mu m^2/s$ **A** The spatial distribution of calcium-dependent ATP release in normal and CF fibroblasts and **B** the temporal distribution of calcium-dependent ATP release in normal and CF fibroblasts

changed. This is due to an imbalance among the various processes of the cell. The same patterns are observed in Fig. 4B and Fig. 6B for the temporal profile of IP_3 and *ATP* release. The IP_3 and *ATP* release profiles reach steady-state simultaneously at 150 *ms*.

Figure 7 depicts the spatiotemporal Ca^{2+}-dependent *ATP* release for the different source amplitude values along with the buffer concentration 5 μM and diffusion coefficient 16 $\mu m^2/s$ under normal and cystic fibrosis conditions. In Fig. 7, it can be seen that the distribution of Ca^{2+}-dependent *ATP* is higher for greater source amplitude values. In Fig. 7A, the *ATP* concentration is higher at $x = 0\,\mu m$, reduces along the spatial axis and converges on 0.1 μM at $x = 10\,\mu m$. From Fig. 7B, it is clear that the *ATP* level achieves a steady state at time $t = 120\,ms$. Further, there is a substantial difference in *ATP* levels between normal and cystic fibrosis patients. The spatiotemporal *ATP* fluxes are greater in cystic fibrosis patients because the Ca^{2+} concentration is 30% higher in *CF* fibroblasts than in normal [77]. The excess *ATP* is dangerous since it can cause fibrotic diseases [9].

The computation has been carried out for Ca^{2+} concentration with varying buffer concentration values in the range $t = 25\,ms$ to $t = 100\,ms$ for *ATP* release in fibroblast cells. The consequences of buffer concentration on *ATP* distribution profile in fibroblast cells concerning time for various buffer values, i.e., $B = 15, 30, 60, 120\,\mu M$, have been displayed in Fig. 8. For $t = 25, 50, 75$ & $100\,ms$, we observe that the increase in buffering reduces the *ATP* concentration in the cell. Thus, in all cases, the fall in *ATP* is lower for the low buffer and higher for the high buffer. Also, *ATP* concentration converges to a minimum of 0.1 μM.

Figure 9 depicts the spatial and temporal Ca^{2+} dependent *ATP* release under normal and cystic fibrosis for a range of buffer associations rates 5 μM. As seen in Fig. 9, the Ca^{2+} dependent *ATP* decreases as the buffer binding rate increases. Higher binding rates bind higher amounts of free calcium, thereby reducing calcium levels in the cell, which signals the *ATP* system to reduce the production of *ATP* in the cell. In Fig. 9A, we observe the alteration in the curves' nonlinear nature. When the association rate of the buffer is high, we observe a fall in *ATP* production at the source and a steep fall in the *ATP* production curves near the source from $x = 0$ to $x = 2\,\mu m$ due to the dominance of calcium-reducing mechanisms weakening the calcium signal feedback to the *ATP* production system and prompting it to reduce *ATP* production. But when the buffer association rates are low, the *ATP* production is higher at the source due to a strong calcium signal caused by a reduction in the dominance of calcium-reducing mechanisms leading to more effect of calcium-elevating mechanisms. There is a substantial difference in ATP levels in normal and *CF* fibroblasts. Ca^{2+} dependent *ATP* is 30% higher in *CF*

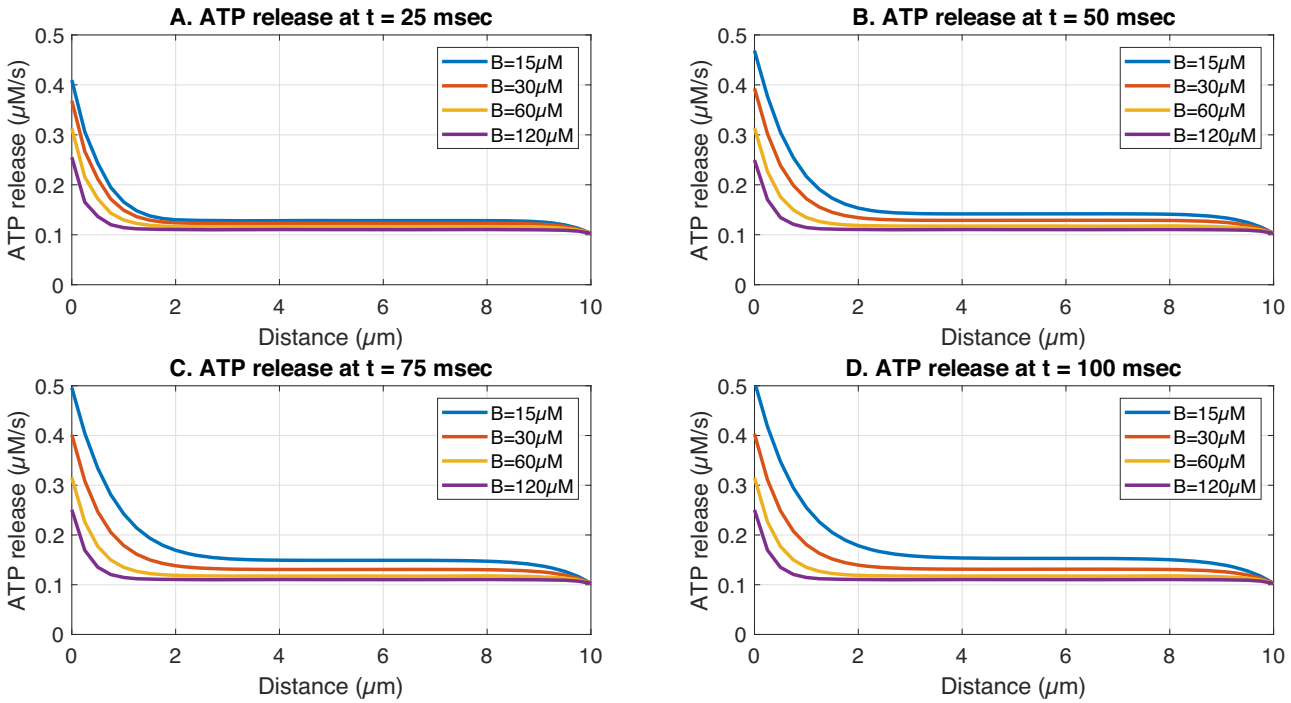

Fig. 8 Ca^{2+} **dependent** *ATP* **distribution at the time** $t = 15, 30, 60, 120\,ms$ **with different buffer concentration for** $D_c = 16\,\mu m^2/s$ **and** $\sigma = 15pA$**. A–D** The spatial distribution of calcium-dependent ATP release with different times for the different buffer concentrations. For a better understanding of the spatiotemporal calcium-regulated ATP synthesis profile

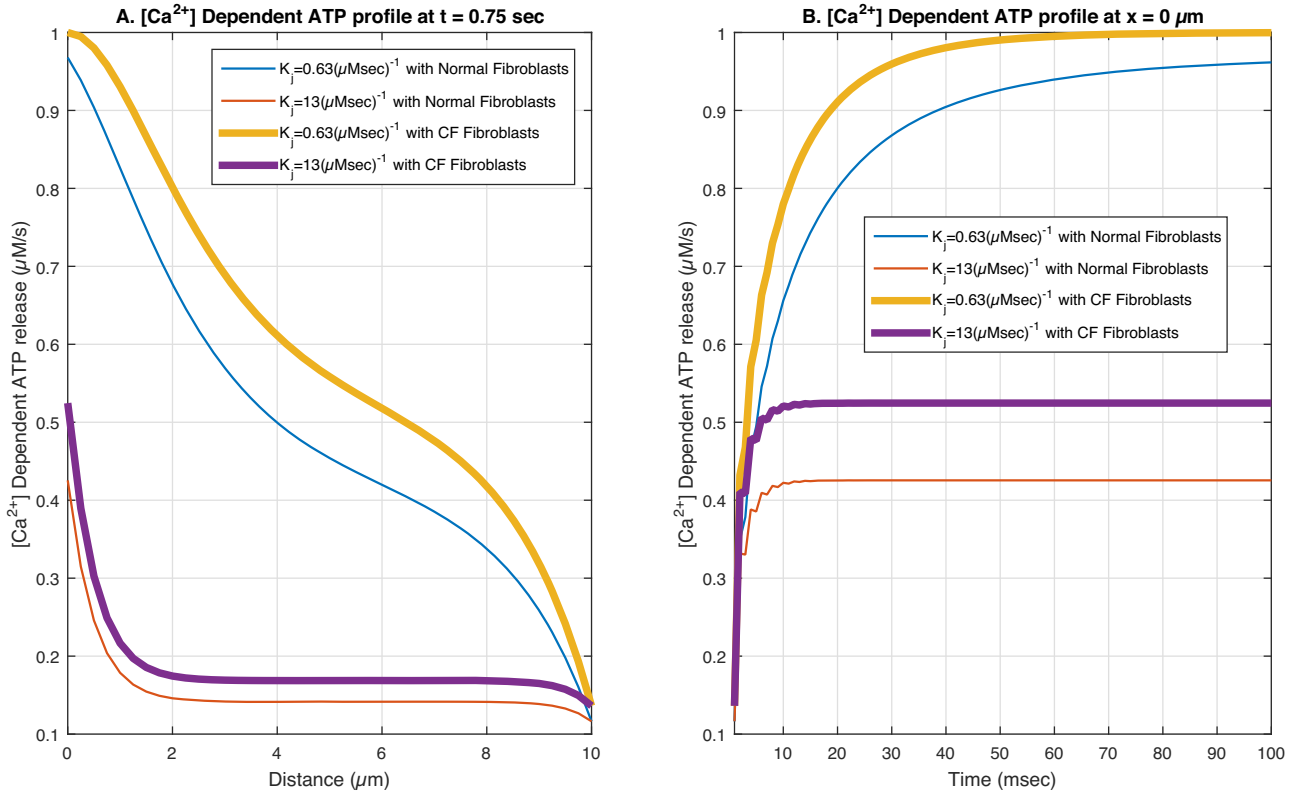

Fig. 9 Ca^{2+} **dependent** *ATP* **release for various association rate for** $[B] = 5\,\mu M$, $D_c = 16\,\mu m^2/s$ **and** $\sigma = 15\,pA$**. A** The spatial distribution of calcium-dependent ATP release and **B** the temporal distribution of calcium-dependent ATP release

Table 2 $[Ca^{2+}]$ profile error analysis at $x = 0\,\mu m$

Time (ms)	30 elements	60 elements	Er	Er%
$t = 50$	1.511546094	1.514033022	0.002486928	0.164258528%
$t = 100$	1.565331190	1.567836631	0.002505440	0.159802394%
$t = 200$	1.539747688	1.572252289	0.002504601	0.159300205%
$t = 500$	1.569776795	1.572281392	0.002504596	0.159296954%
$t = 1000$	1.569776795	1.572281392	0.002504596	0.159296954%

Table 3 $[IP_3]$ profile error analysis at $x = 0.25\,\mu m$

Time (ms)	30 elements	60 elements	Er	Er%
$t = 50$	2.906796826	2.932241449	0.025444623	0.875349221%
$t = 100$	2.905471051	2.929648987	0.024177936	0.832152003%
$t = 200$	2.90529478	2.929025631	0.023730850	0.816813852%
$t = 500$	2.905289762	2.928963807	0.023674045	0.814860031%
$t = 1000$	2.905289761	2.928963602	0.023673841	0.814852992%

Table 4 Comparison of Ca^{2+} profile with Wagner et al. [68] & Pawar and Pardasani [61, 62] at $t = 50\,s$

Position (μm)	$[Ca^{2+}]$ Wagner et al. [68]	$[Ca^{2+}]$ Pawar [61, 62]	$[Ca^{2+}]$ (Our results)
$x = 0$	1.35000000000	1.349818367318	1.3494422979
$x = 2$	1.19112370933	1.192989368534	1.1298818160
$x = 4$	1.01615701363	1.016076559106	1.0094515370
$x = 6$	0.79585798185	0.795809556080	0.8897183280
$x = 8$	0.50327133155	0.503248604412	0.6533498430
$x = 10$	0.10000000000	0.100000000000	0.1000000000

Table 5 Comparison of IP_3 profile with Wagner et al. [68] & Pawar and Pardasani [61, 62] at $t = 50\,s$

Position μm	$[IP_3]$ Wagner et al. [68]	$[IP_3]$ Pawar [61, 62]	$[IP_3]$ (Our results)
$x = 0$	0.500000000	0.500000000	0.500000000
$x = 2$	0.431214742	0.431787350	0.431261675
$x = 4$	0.345841649	0.363691496	0.345906691
$x = 6$	0.294906295	0.295702458	0.294963669
$x = 8$	0.227295867	0.227809393	0.227328888
$x = 10$	0.160000000	0.160000000	0.160000000

fibroblasts than in normal. This process occurs if the rate of association is high.

Error Estimation

The absolute comparative error and its percentage in a fibroblast cell have been estimated and shown in Tables 2 and 3. The model's accuracy for Ca^{2+} and IP_3 is 99.84019761%, 99.84070305%, 99.84070305 and 99.167848%, 99.18513997%, 99.18514701% for the time ($t = 50, 100, 200, 500$ & 1000) ms respectively. As a result, the absolute worst-case scenario for the error rate of this model is 0.16%, while 99.84% is the utmost best-case scenario for its accuracy. Because the grid sensitivity is essentially nonexistent, this strongly argues that the solution is not grid-reliant.

Validation

For varied parameters, the profiles of Ca^{2+} and IP_3 levels were produced. For the Ca^{2+} profile, the amount of buffer was set at $0.0\,\mu M$, while the source inflow was set at $2.46\,pA$. The results of the Ca^{2+} and IP_3 in the current model for $t = 50\,s$ are compared with the findings of Pawar and Pardasani [61, 62] & Wagner et al. [68] as depicts in Tables 4 and 5. It appears that the proposed study's results are very similar to those derived from previous studies.

Stability Analysis

We determined the spectral radius for the stability investigation, and if the radius of the spectrum is equal to or below one, the system is considered stable [79]. In this specific case, the spectral radius was determined to be 0.9853, so it's <1, indicating that the calculated result is stable.

Conclusion

A model is developed and successfully implemented to explore the consequences of disruptions in coupled IP_3 and Ca^{2+} dynamics on ATP generation in a fibroblast cell.

Disruptions in the interdependent IP_3 and Ca^{2+} levels can be induced by the failure of mechanisms such as buffering and the *serca* pump. As a result of some disorder in these processes, high amounts of source input, association rate and higher buffer values were investigated. These perturbations significantly impacted Ca^{2+} and IP_3 dynamics regulating *ATP* generation. For obtaining numerical solutions under various situations, the finite element and Crank Nicholson were used. In light of the unexpected results, the following conclusions are reached:

1. When the source of the inflow is substantial and the *serca* and buffer are low, the calcium concentration rises, resulting in increased IP_3 concentrations in fibroblast cells.
2. High buffer levels cause irregularities because of oscillations in the Ca^{2+} distributions in fibroblast cells.
3. An rise in Ca^{2+} concentration results from an increase in IP_3 levels, which in turn boosts *ATP* synthesis.

The fundamental findings described above are supported by biological evidence. In addition, the results of the stability analysis, error analysis, and validation procedures used in the current study suggest that the suggested model is appropriate and effective for the inquiry at hand. Furthermore, the following innovative deductions and inferences drawn from the numerical data are provided:

1. The large volumes of source input result in higher Ca^{2+} levels, which boosts the *ATP* release in normal fibroblast and cystic fibrosis fibroblast. These changes in *ATP* signalling can result in fibrotic disorders like fibrosis [46].
2. The presence of buffers decreases Ca^{2+} and IP_3 levels in normal fibroblast and cystic fibrosis fibroblast and lowers the rate of selective death of fibroblasts. insufficient quantities of *EGTA* and calmodulin buffers can lead to cystic fibrosis [77].
3. When buffer is low, Ca^{2+} levels rise, increasing *ATP* release in fibroblasts as well as cystic fibrosis fibroblast. The increase in Ca^{2+} and IP_3 concentrations within the cell promotes the loss of fibroblast cells, which leads to cancer [80].
4. Increased *ATP* production is risky since it might result in fibrotic diseases. One more novelty of the results is the spatiotemporal *ATP* production are greater in cystic fibrosis patients because the Ca^{2+} concentration is 30% higher in *CF* fibroblasts than in normal fibroblasts [77].

Disruptions in numerous generative processes of IP_3 and Ca^{2+}dynamics might result in altered *ATP* synthesis, leading to various fibrotic diseases. Lowered buffering capacity, impaired buffer association performance, high levels of source inflow, and fluctuations in IP_3 levels can induce increases in free Ca^{2+} levels and *ATP* generation, which is the cause of cystic fibrosis when there is a discrepancy between adenosine triphosphate production and its metabolism.

The results concur with biological realities. In the current work, the *FEM* technique is extremely successful. The model proposed sheds light on the underlying processes of Ca^{2+} and IP_3 dynamics that cause an increase in *ATP* production, which has been identified as a factor causing cytotoxicity and contributing to the development of cystic fibrosis. The findings highlight the challenge of determining the correct constitutive procedure of IP_3 and Ca^{2+} dynamics, crucial in *ATP* production alterations in fibrosis. Although many questions remain unanswered, the results from studying the relationships between the constitutive processes of IP_3 and Ca^{2+} dynamics and *ATP* synthesis can pave the way to address the aforementioned challenges.

Author contributions We, the writers, contributed equally to this paper regarding problem design, solution, literature review, and result interpretation. MATLAB code is developed by the first author.

Compliance with ethical standards

Conflict of interest The authors declare no competing interests.

Appendix

The shape function is assumed

$$m0^{(e)} = q_1^{(e)} + q_2^{(e)} x. \tag{A1}$$

$$n0^{(e)} = r_1^{(e)} + r_2^{(e)} x. \tag{A2}$$

$$m0^{(e)} = X^T \times q^{(e)},\ n0^{(e)} = X^T \times r^{(e)}. \tag{A3}$$

Where,

$$S^T = [1\ \ x],\ q^{(e)^T} = [q_1^{(e)}\ q_2^{(e)}]\ and\ r^{(e)^T} = [r_1^{(e)}\ r_2^{(e)}]. \tag{A4}$$

In equation (A3), substitute the nodal conditions, we obtain

$$\overline{m}0^{(e)} = X^{(e)} \times q^{(e)},\ and\ \overline{n}0^{(e)} = X^{(e)} \times r^{(e)}. \tag{A5}$$

Where,

$$\overline{m}0^{(e)} = \begin{bmatrix} m0_i \\ m0_j \end{bmatrix},\ \overline{v}^{(e)} = \begin{bmatrix} n0_i \\ n0_j \end{bmatrix}\ and\ X^{(e)} = \begin{bmatrix} 1 & x_i \\ 1 & x_j \end{bmatrix}. \tag{A6}$$

By the equations (A5), we have

$$q^{(e)} = (Y^{(e)}) \times \overline{m}0^{(e)} \;\&\; r^{(e)} = (Y^{(e)}) \times \overline{n}0^{(e)}. \tag{A7}$$

Where,

$$Y^{(e)} = \frac{1}{X^{(e)}}. \tag{A8}$$

Substituting the values of $q^{(e)}$ & $r^{(e)}$ in equation (A3), we obtained

$$m0^{(e)} = X^T \times Y^{(e)}\, \overline{m}0^{(e)} \; and \; n0^{(e)} = X^T \times Y^{(e)}\, \overline{n}0^{(e)}. \tag{A9}$$

The partial differential equations (1) and (7) can be written as,

$$I_1^{(e)} = I_{ao1}^{(e)} - I_{bo1}^{(e)} + I_{co1}^{(e)} - I_{do1}^{(e)} + I_{eo1}^{(e)} - I_{fo1}^{(e)} - I_{go1}^{(e)}. \tag{A10}$$

Where

$$I_{ao1}^{(e)} = \int_{x_i}^{x_j} \left[\left[\frac{\partial m0^{(e)}}{\partial x} \right]^2 \right] dx, \tag{A11}$$

$$I_{bo1}^{(e)} = \frac{d}{dx} \int_{x_i}^{x_j} \left[\frac{m0^{(e)}}{D_c} \right] dx, \tag{A12}$$

$$I_{co1}^{(e)} = \frac{V_{IP_3R}}{D_c F_c} \int_{x_i}^{x_j} \left[\alpha m0^{(e)} + \beta n0^{(e)} + \gamma \right] dx, \tag{A13}$$

$$I_{do1}^{(e)} = \frac{V_{serca}}{D_c F_c} \int_{x_i}^{x_j} \left[k m0^{(e)} - \eta \right] dx, \tag{A14}$$

$$I_{eo1}^{(e)} = \frac{V_{leak}}{D_c F_c} \int_{x_i}^{x_j} \left[[Ca^{2+}]_{ER} - m0^{(e)} \right] dx, \tag{A15}$$

$$I_{fo1}^{(e)} = \frac{K^-}{D_c} \int_{x_i}^{x_j} \left[m0^{(e)} - [Ca^{2+}]_{\infty} \right] dx, \tag{A16}$$

$$I_{go1}^{(e)} = f^{(e)} \left[\frac{\sigma}{D_c} \right]_{x=0}. \tag{A17}$$

$$I_2^{(e)} = I_{ao2}^{(e)} - I_{bo2}^{(e)} + I_{co2}^{(e)} - I_{do2}^{(e)}. \tag{A18}$$

$$I_{ao2}^{(e)} = \int_{x_i}^{x_j} \left[\left[\frac{\partial n0^{(e)}}{\partial x} \right]^2 \right] dx, \tag{A19}$$

$$I_{bo2}^{(e)} = \frac{d}{dx} \int_{x_i}^{x_j} \left[\frac{n0^{(e)}}{D_I} \right] dx, \tag{A20}$$

$$I_{co2}^{(e)} = \frac{V_{prod}}{D_I F_c} \int_{x_i}^{x_j} \left[\mu m0^{(e)} + \tau \right] dx, \tag{A21}$$

$$I_{do2}^{(e)} = \frac{\lambda}{D_I F_c} \int_{x_i}^{x_j} \left[\delta m0^{(e)} + \zeta n0^{(e)} + \gamma_2 \right] dx. \tag{A22}$$

Linearizing IP_3 and Ca^{2+} dynamics yields the quantity of $\delta, \gamma, k, \eta, \mu, \zeta, \gamma_2, \alpha, \beta$ and τ. The equations after calculation and boundary circumstances are as follows.

$$\frac{dI_1}{d\overline{m}0^{(e)}} = \sum_{e=1}^{N} \left[\overline{Q}^{(e)} \frac{dI_1^{(e)}}{d\overline{m}0^{(e)}} \overline{Q}^{(e)^T} \right] = 0. \tag{A23}$$

$$\frac{dI_2}{d\overline{n}0^{(e)}} = \sum_{e=1}^{N} \left[\overline{Q}^{(e)} \frac{dI_2^{(e)}}{d\overline{n}0^{(e)}} \overline{Q}^{(e)^T} \right] = 0. \tag{A24}$$

Where,

$$\frac{dI_1^{(e)}}{d\overline{m}0^{(e)}} = \frac{dI_{ao1}^{(e)}}{d\overline{m}0^{(e)}} + \frac{d}{dt}\left[\frac{dI_{bo1}^{(e)}}{d\overline{m}0^{(e)}} \right] + \frac{dI_{co1}^{(e)}}{d\overline{m}0^{(e)}} + \frac{dI_{do1}^{(e)}}{d\overline{m}0^{(e)}} - \frac{dI_{eo1}^{(e)}}{d\overline{m}0^{(e)}} - \frac{dI_{fo1}^{(e)}}{d\overline{m}0^{(e)}}. \tag{A25}$$

$$\frac{dI_2^{(e)}}{d\overline{n}0^{(e)}} = \frac{dI_{ao2}^{(e)}}{d\overline{n}0^{(e)}} + \frac{d}{dt}\left[\frac{dI_{bo2}^{(e)}}{d\overline{n}0^{(e)}} \right] + \frac{dI_{co2}^{(e)}}{d\overline{n}0^{(e)}} + \frac{dI_{d2}^{(e)}}{d\overline{n}0^{(e)}} - \frac{dI_{eo2}^{(e)}}{d\overline{n}0^{(e)}}. \tag{A26}$$

$$\overline{M}^{(el)} = \begin{bmatrix} 0 & 0 \\ . & . \\ 0 & 0 \\ 1 & 0 \\ 0 & 1 \\ 0 & 0 \\ . & . \\ 0 & 0 \end{bmatrix}, \overline{u} = \begin{bmatrix} u_1 \\ u_2 \\ u_3 \\ . \\ . \\ . \\ u_{30} \\ u_{31} \end{bmatrix} and \; \overline{v} = \begin{bmatrix} v_1 \\ v_2 \\ v_3 \\ . \\ . \\ . \\ v_{30} \\ v_{31} \end{bmatrix}. \tag{A27}$$

$$[A]_{62\times62} \begin{bmatrix} \left[\frac{\partial \overline{u}}{\partial t}\right]_{31\times1} \\ \left[\frac{\partial \overline{v}}{\partial t}\right]_{31\times1} \end{bmatrix} + [B]_{62\times62} \begin{bmatrix} [\overline{u}]_{31\times1} \\ [\overline{v}]_{31\times1} \end{bmatrix} = [F]_{62\times1}. \tag{A28}$$

We utilize the statistically stable Crank Nicholson Method on the matrices A and B to determine the time derivative using the Finite Element Approach, and the force vector is F. To solve the resultant system of equations, the Gaussian Elimination Method is utilized.

References

1. Berridge, M., Lipp, P., & Bootman, M. (1999). Calcium signalling. *Current Biology*, *9*, R157–R159.
2. Capote, L. A., Perez, R. M., & Lymperopoulos, A. (2015). GPCR signaling and cardiac function. *European Journal of Pharmacology*, *763*, 143–148.
3. Berridge, M. J., & Irvine, R. F. (1984). Inositol trisphosphate, a novel second messenger in cellular signal transduction. *Nature*, *312*, 315–321.
4. Bootman, M. D., Fearnley, C., Smyrnias, I., MacDonald, F., & Roderick, H. L. (2009). An update on nuclear calcium signalling. *Journal Of Cell Science*, *122*, 2337–2350.
5. Bootman, M. D., & Berridge, M. J. (1995). The elemental principles of calcium signaling. *Cell*, *83*, 675–678.
6. Chen, J.-B., et al. (2012). Adenosine-5-triphosphate up-regulates proliferation of human cardiac fibroblasts. *British Journal Of Pharmacology*, *166*, 1140–1150.
7. Perera, L. M. B., et al. (2019). The regulation of skin fibrosis in systemic sclerosis by extracellular atp via p2y2 purinergic receptor. *Journal Of Investigative Dermatology*, *139*, 890–899.
8. Smith, D. G., Mills, W. J., Steen, R. G., & Williams, D. (1999). Levels of high energy phosphate in the dorsal skin of the foot in normal and diabetic adults: the role of 31p magnetic resonance spectroscopy and direct quantification with high pressure liquid chromatography. *Foot & Ankle International*, *20*, 258–262.
9. Riteau, N., et al. (2010). Extracellular atp is a danger signal activating p2x7 receptor in lung inflammation and fibrosis. *American Journal of Respiratory and Critical Care Medicine*, *182*, 774–783.
10. Lu, D., Soleymani, S., Madakshire, R., & Insel, P. A. (2012). Atp released from cardiac fibroblasts via connexin hemichannels activates profibrotic p2y2 receptors. *The FASEB Journal*, *26*, 2580.
11. Pelleg, A. (2021). Extracellular adenosine 5-triphosphate in pulmonary disorders. *Biochemical Pharmacology*, *187*, 114319.
12. Goncalves, R., et al. (2006). The role of purinergic p2x7 receptors in the inflammation and fibrosis of unilateral ureteral obstruction in mice. *Kidney International*, *70*, 1599–1606.
13. Menon, S. N., et al. (2012). Modelling the interaction of keratinocytes and fibroblasts during normal and abnormal wound healing processes. *Proceedings of the Royal Society B: Biological Sciences*, *279*, 3329–3338.
14. Droniou, J., Flegg, J. A., & Remesan, G. C. (2020). Numerical solution of a two dimensional tumour growth model with moving boundary. *Journal of Scientific Computing*, *85*, 1–31.
15. Simpson, M. J., Lo, K.-Y., & Sun, Y.-S. (2017). Quantifying the roles of random motility and directed motility using advection-diffusion theory for a 3t3 fibroblast cell migration assay stimulated with an electric field. *BMC Systems Biology*, *11*, 1–9.
16. Michell, R. H. (1975). Inositol phospholipids and cell surface receptor function. *Biochimica et Biophysica Acta (BBA)-Reviews on Biomembranes*, *415*, 81–147.
17. Fogelson, A. L., & Zucker, R. S. (1985). Presynaptic calcium diffusion from various arrays of single channels. implications for transmitter release and synaptic facilitation. *Biophysical Journal*, *48*, 1003–1017.
18. Jafri, M., & Keizer, J. (1995). On the roles of calcium diffusion, calcium buffers, and the endoplasmic reticulum in ip3-induced calcium waves. *Biophysical Journal*, *69*, 2139–2153.
19. Smith, G. D., Wagner, J., & Keizer, J. (1996). Validity of the rapid buffering approximation near a point source of calcium ions. *Biophysical Journal*, *70*, 2527–2539.
20. Torres, J. J., et al. (2004). Modeling action potential generation and propagation in nrk fibroblasts. *American Journal of Physiology-Cell Physiology*, *287*, C851–C865.
21. Kusters, J., et al. (2007). Hysteresis and bistability in a realistic cell model for calcium oscillations and action potential firing. *Physical Review Letters*, *98*, 098107.
22. Wagner, J., & Keizer, J. (1994). Effects of rapid buffers on calcium diffusion and calcium oscillations. *Biophysical Journal*, *67*, 447–456.
23. Kotwani, M., Adlakha, N., & Mehta, M. (2012). Numerical model to study calcium diffusion in fibroblasts cell for one dimensional unsteady state case. *Applied Mathematical Sciences*, *6*, 5063–5072.
24. Kotwani, M., & Adlakha, N. (2017). Modeling of endoplasmic reticulum and plasma membrane calcium uptake and release fluxes with excess buffer approximation (eba) in fibroblast cell. *International Journal of Computational Materials Science and Engineering*, *6*, 1750004.
25. Sun, G.-X., Wang, L.-J., Xiang, C., & Qin, K.-R. (2013). A dynamic model for intracellular calcium response in fibroblasts induced by electrical stimulation. *Mathematical Biosciences*, *244*, 47–57.
26. Manhas, N., & Pardasani, K. (2014). Modelling mechanism of calcium oscillations in pancreatic acinar cells. *Journal of Bioenergetics and Biomembranes*, *46*, 403–420.
27. Manhas, N., & Pardasani, K. R. (2014). Mathematical model to study ip3 dynamics dependent calcium oscillations in pancreatic acinar cells. *Journal of Medical Imaging and Health Informatics*, *4*, 874–880.
28. Jha, A., & Adlakha, N. (2014). Analytical solution of two dimensional unsteady state problem of calcium diffusion in a neuron cell. *Journal of Medical Imaging and Health Informatics*, *4*, 547–553.
29. Joshi, H., & Jha, B. K. (2020). Fractional-order mathematical model for calcium distribution in nerve cells. *Computational and Applied Mathematics*, *39*, 1–22.
30. Joshi, H., & Jha, B. K. (2021). Chaos of calcium diffusion in parkinson's infectious disease model and treatment mechanism via hilfer fractional derivative. *Mathematical Modelling and Numerical Simulation with Applications*, *1*, 84–94.
31. Jha, A., & Adlakha, N. (2015). Two-dimensional finite element model to study unsteady state calcium diffusion in neuron involving er leak and serca. *International Journal of Biomathematics*, *8*, 1550002.
32. Jha, A., Adlakha, N., & Jha, B. K. (2016). Finite element model to study effect of sodium-calcium exchangers and source geometry on calcium dynamics in a neuron cell. *Journal of Mechanics in Medicine and Biology*, *16*, 1650018.
33. Tewari, V., Tewari, S., & Pardasani, K. (2011). A model to study the effect of excess buffers and na+ ions on ca2+ diffusion in neuron cell. *International Journal of Bioengineering and Life Sciences*, *5*, 251–256.
34. Pathak, K., & Adlakha, N. (2016). Finite element model to study two dimensional unsteady state calcium distribution in cardiac myocytes. *Alexandria Journal of Medicine*, *52*, 261–268.
35. Naik, P. A., & Pardasani, K. R. (2013). One dimensional finite element method approach to study effect of ryanodine receptor and serca pump on calcium distribution in oocytes. *Journal of Multiscale Modelling*, *5*, 1350007.
36. Naik, P. A., & Pardasani, K. R. (2015). One dimensional finite element model to study calcium distribution in oocytes in presence of vgcc, ryr and buffers. *Journal of Medical Imaging and Health Informatics*, *5*, 471–476.
37. Naik, P. A., & Pardasani, K. R. (2019). Three-dimensional finite element model to study effect of ryr calcium channel, er leak and serca pump on calcium distribution in oocyte cell. *International Journal of Computational Methods*, *16*, 1850091.
38. Kotwani, M., Adlakha, N., & Mehta, M. (2014). Finite element model to study the effect of buffers, source amplitude and source geometry on spatio-temporal calcium distribution in fibroblast

cell. *Journal of Medical Imaging and Health Informatics*, *4*, 840–847.
39. Kothiya, A., & Adlakha, N. (2022). Model of calcium dynamics regulating ip3 and atp production in a fibroblast cell. *Advances in Systems Science and Applications*, *22*, 106–125.
40. Jha, B. K., Adlakha, N., & Mehta, M. (2014). Two-dimensional finite element model to study calcium distribution in astrocytes in presence of excess buffer. *International Journal of Biomathematics*, *7*, 1450031.
41. Jagtap, Y., & Adlakha, N. (2018). Simulation of buffered advection diffusion of calcium in a hepatocyte cell. *Mathematical Biology and Bioinformatics*, *13*, 609–619.
42. Stamatakis, M., & Mantzaris, N. V. (2006). Modeling of atp-mediated signal transduction and wave propagation in astrocytic cellular networks. *Journal of Theoretical Biology*, *241*, 649–668.
43. Allison, A., Hovi, T., Watts, R. & Webster, A. The role of de novo purine synthesis in lymphocyte transformation. *Purine and Pyrimidine Metabolism* 207–224 (1977).
44. Scantland, S., et al. (2014). The adenosine salvage pathway as an alternative to mitochondrial production of atp in maturing mammalian oocytes. *Biology of Reproduction*, *91*, 75–1.
45. Zhao, R.-Z., Jiang, S., Zhang, L., & Yu, Z.-B. (2019). Mitochondrial electron transport chain, ros generation and uncoupling. *International Journal of Molecular Medicine*, *44*, 3–15.
46. Bryan, A., Sabanov, V., Thoroed, S., & Doroshenko, P. (2000). Dual role of atp in supporting volume-regulated chloride channels in mouse fibroblasts. *Biochimica et Biophysica Acta (BBA)-Biomembranes*, *1468*, 63–72.
47. Miyoshi, N., Oubrahim, H., Chock, P. B., & Stadtman, E. R. (2006). Age-dependent cell death and the role of atp in hydrogen peroxide-induced apoptosis and necrosis. *Proceedings of the National Academy of Sciences*, *103*, 1727–1731.
48. Kotwal, G. J., Sarojini, H., & Chien, S. (2015). Pivotal role of atp in macrophages fast tracking wound repair and regeneration. *Wound Repair and Regeneration*, *23*, 724–727.
49. Kumar, H., Naik, P. A., & Pardasani, K. R. (2018). Finite element model to study calcium distribution in t lymphocyte involving buffers and ryanodine receptors. *Proceedings of the National Academy of Sciences, India Section A: Physical Sciences*, *88*, 585–590.
50. Jagtap, Y., & Adlakha, N. (2018). Finite volume simulation of two dimensional calcium dynamics in a hepatocyte cell involving buffers and fluxes. *Communications in Mathematical Biology and Neuroscience*, *2018*, Article–ID.
51. Joshi, H., Yavuz, M., & Stamova, I. (2023). Analysis of the disturbance effect in intracellular calcium dynamic on fibroblast cells with an exponential kernel law. *Bulletin of Biomathematics*, *1*, 24–39.
52. Bonora, M., et al. (2012). Atp synthesis and storage. *Purinergic Signalling*, *8*, 343–357.
53. Nazaret, C., Heiske, M., Thurley, K., & Mazat, J.-P. (2009). Mitochondrial energetic metabolism: a simplified model of tca cycle with atp production. *Journal of Theoretical Biology*, *258*, 455–464.
54. Cortassa, S., Aon, M. A., Marbán, E., Winslow, R. L., & O'Rourke, B. (2003). An integrated model of cardiac mitochondrial energy metabolism and calcium dynamics. *Biophysical Journal*, *84*, 2734–2755.
55. Tarasov, A. I., Griffiths, E. J., & Rutter, G. A. (2012). Regulation of atp production by mitochondrial ca2+. *Cell Calcium*, *52*, 28–35.
56. Jagtap, Y., & Adlakha, N. (2019). Numerical study of one-dimensional buffered advection–diffusion of calcium and ip3 in a hepatocyte cell. *Network Modeling Analysis in Health Informatics and Bioinformatics*, *8*, 1–9.
57. Singh, N., & Adlakha, N. (2019). A mathematical model for interdependent calcium and inositol 1, 4, 5-trisphosphate in cardiac myocyte. *Network Modeling Analysis in Health Informatics and Bioinformatics*, *8*, 1–15.
58. Pawar, A., & Pardasani, K. R. (2022). Simulation of disturbances in interdependent calcium and β-amyloid dynamics in the nerve cell. *The European Physical Journal Plus*, *137*, 1–23.
59. Pawar, A. & Pardasani, K. R. Study of disorders in regulatory spatiotemporal neurodynamics of calcium and nitric oxide. *Cognitive Neurodynamics* 1–22 (2022).
60. Pawar, A., & Pardasani, K. R. (2023). Computational model of calcium dynamics-dependent dopamine regulation and dysregulation in a dopaminergic neuron cell. *The European Physical Journal Plus*, *138*, 1–19.
61. Pawar, A. & Pardasani, K. R. (2022). Effect of disturbances in neuronal calcium and ip3 dynamics on β-amyloid production and degradation. *Cognitive Neurodynamics*, *17*, 239–256.
62. Pawar, A., & Raj Pardasani, K. (2022). Effects of disorders in interdependent calcium and ip3 dynamics on nitric oxide production in a neuron cell. *The European Physical Journal Plus*, *137*, 1–19.
63. Pawar, A. & Pardasani, K. R. (2023). Mechanistic insights of neuronal calcium and ip3 signaling system regulating atp release during ischemia in progression of alzheimer's disease. *European Biophysics Journal*, *52*, 153–173.
64. Kothiya, A. B. & Adlakha, N. (2023). Cellular nitric oxide synthesis is affected by disorders in the interdependent calcium and ip3 dynamics during cystic fibrosis disease. *Journal of Biological Physics*, *49*, 133–158.
65. Singh, N. & Adlakha, N. Effect of source geometry on interdependent calcium and inositol 1; 4; 5-trisphosphate dynamics in a cardiac myocyte cell. In *Mathematical Modelling and Scientific Computing with Applications: ICMMSC 2018, Indore, India, July 19–21*, 75–83, Singapore (Springer, 2020).
66. Vaishali & Adlakha, N. Disturbances in system dynamics of c a 2+ and ip 3 perturbing insulin secretion in a pancreatic β-cell due to type-2 diabetes. *Journal of Bioenergetics and Biomembranes, 55,* 151–167 (2023).
67. Kothiya, A. & Adlakha, N. (2023). Simulation of biochemical dynamics of calcium and plc in fibroblast cell. *Journal of Bioenergetics and Biomembranes*, *55*, 267–287.
68. Wagner, J., et al. (2004). A wave of ip3 production accompanies the fertilization calcium wave in the egg of the frog, xenopus laevis: theoretical and experimental support. *Cell Calcium*, *35*, 433–447.
69. Keizer, J., & De Young, G. (1994). Simplification of a realistic model of ip3-induced calcium oscillations. *Journal of Theoretical Biology*, *166*, 431–442.
70. Bugrim, A., Fontanilla, R., Eutenier, B. B., Keizer, J., & Nuccitelli, R. (2003). Sperm initiate a ca2+ wave in frog eggs that is more similar to ca2+ waves initiated by ip3 than by ca2+. *Biophysical Journal*, *84*, 1580–1590.
71. Sims, C. E., & Allbritton, N. L. (1998). Metabolism of inositol 1, 4, 5-trisphosphate and inositol 1, 3, 4, 5-tetrakisphosphate by the oocytes of xenopus laevis. *Journal of Biological Chemistry*, *273*, 4052–4058.
72. Brown, S.-A., Morgan, F., Watras, J., & Loew, L. M. (2008). Analysis of phosphatidylinositol-4, 5-bisphosphate signaling in cerebellar purkinje spines. *Biophysical Journal*, *95*, 1795–1812.
73. Dupont, G., Swillens, S., Clair, C., Tordjmann, T., & Combettes, L. (2000). Hierarchical organization of calcium signals in hepatocytes: from experiments to models. *Biochimica et Biophysica Acta (BBA)-Molecular Cell Research*, *1498*, 134–152.
74. Smith, G. D. (1996). Analytical steady-state solution to the rapid buffering approximation near an open calcium channel. *Biophysical Journal*, *71*, 3064–3072.
75. Tewari, S., & Pardasani, K. (2010). Finite element model to study two dimensional unsteady state cytosolic calcium diffusion in

presence of excess buffers. *IAENG International Journal of Applied Mathematics*, *40*, 108–112.
76. Fink, C. C., et al. (2000). An image-based model of calcium waves in differentiated neuroblastoma cells. *Biophysical Journal*, *79*, 163–183.
77. Gnegy, M. E., Erickson, R. P., & Markovac, J. (1981). Increased calmodulin in cultured skin fibroblasts from patients with cystic fibrosis. *Biochemical Medicine*, *26*, 294–298.
78. Shapiro, B. L., Feigal, R. J., Laible, N. J., Biros, M. H., & Warwick, W. J. (1978). Doubling time α-aminoisobutyrate transport and calcium exchange in cultured fibroblasts from cystic fibrosis and control subjects. *Clinica Chimica Acta*, *82*, 125–131.
79. Öziş, T., Aksan, E., & Özdeş, A. (2003). A finite element approach for solution of burgers' equation. *Applied Mathematics and Computation*, *139*, 417–428.
80. Housey, G. M., et al. (1988). Overproduction of protein kinase c causesdisordered growth control in rat fibroblasts. *Cell*, *52*, 343–354.